Article

Photonic radar for contactless vital sign detection

Ziqian Zhang [1,2], Yang Liu [1,2,4] ✉, Tegan Stephens [3] &
Benjamin J. Eggleton [1,2] ✉

Vital sign detection is used across ubiquitous scenarios in medical and health settings, and contact and wearable sensors have been widely deployed. However, they are unsuitable for patients with burn wounds or infants with insufficient areas for attachment. Contactless detection can be achieved using camera imaging, but it is susceptible to ambient light conditions and has privacy concerns. Here we report a photonic radar for non-contact vital sign detection to overcome these challenges. This photonic radar can achieve millimetre-level range resolution based on synthesized radar signals with a bandwidth of up to 30 GHz. The high resolution of the radar system enables accurate respiratory detection from breathing simulators and a cane toad as a human proxy. Moreover, we demonstrate that the optical signals generated from the proposed system can enable vital sign detection based on light detection and ranging (LiDAR). This demonstration reveals the potential of a sensor-fusion architecture that can combine the complementary features of radar and LiDAR to achieve improved sensing accuracy and system resilience. The work provides a technical basis for contactless and high-resolution vital sign detection to meet the increasing demands of future medical and healthcare applications.

Vital signs—a group of clinical measurements reflecting essential body functions—are used as diagnostic parameters for monitoring medical and health conditions. Vital sign detection is widely employed across ubiquitous scenarios, including intensive care units for patients with critical health conditions, aged-care facilities for day-and-night health monitoring to prevent medical emergencies in unattended patients and vehicles to determine the occurrence of driver drowsiness[1,2]. Conventional vital sign detection relies on contact-based devices, such as pulse oximeters, which use electrodes to detect weak electrical changes resulting from cardiac contractions (electrocardiography), and smartwatches, based on the intensity variation of infrared probe light caused by blood flow and volume changes (photoplethysmography)[3]. Although widely deployed, contact-based methods can cause discomfort when used in round-the-clock monitoring[4–6].

Despite improved user experience with wearable sensors located in bands or clothes, they are unsuitable for patients with burn wounds or skin irritations, and in infants with an insufficient area for attachment[7]. Non-contacting methods based on optical sensors have been explored, for instance, using cameras to track certain body regions of interest[8–10]. However, camera-based systems (including infrared and conventional cameras) are sensitive to skin colour and lighting conditions[11]. Such systems typically rely on complex computing algorithms and infrared camera-generated thermal videos, and often have limited resolution[12]. Additionally, the high resolution of some camera-based systems can lead to privacy concerns[13–15], particularly when invasive monitoring practices are involved and insufficient security measures exist within cloud computing and data-storage infrastructures.

[1]Institute of Photonics and Optical Science (IPOS), School of Physics, The University of Sydney, Camperdown, New South Wales, Australia. [2]The University of Sydney Nano Institute (Sydney Nano), The University of Sydney, Camperdown, New South Wales, Australia. [3]Bird and Exotics Veterinarian, Waterloo, New South Wales, Australia. [4]Present address: Institute of Physics, Swiss Federal Institute of Technology Lausanne (EPFL), Lausanne, Switzerland. ✉e-mail: yang.liu@sydney.edu.au; benjamin.eggleton@sydney.edu.au
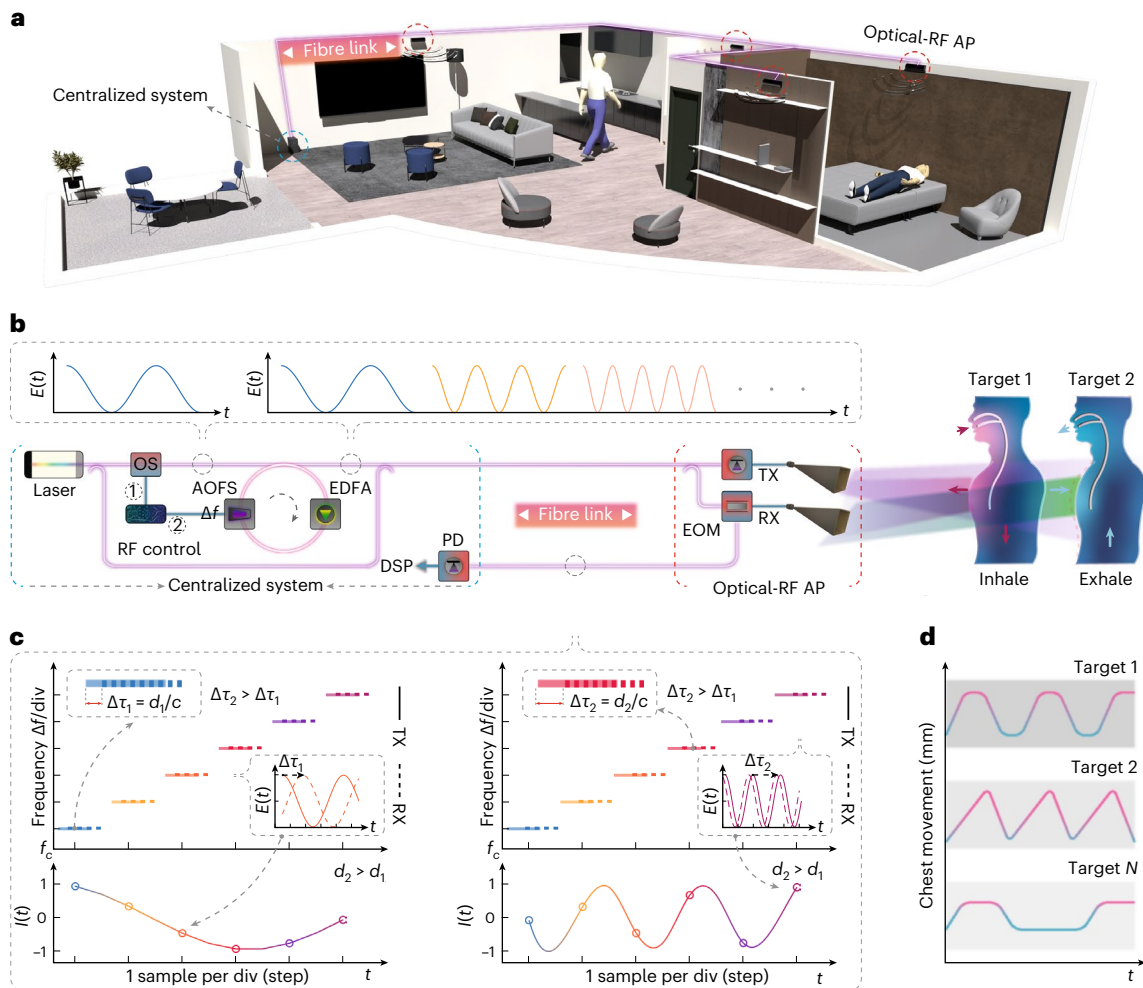
**Fig. 1 | A photonics-enabled radar system for contactless vital sign detection.** **a**, Conceptual drawing of the vital sign radar with distributed sensing access points (APs) enabled by low-loss fibre and a centralized, photonics-assisted radar platform. **b**, Schematic of the demonstrated photonic radar for vital sign detection based on a frequency-shifting (FS) fibre cavity with its optical input and output signals shown on the top. A seed pulse at a single frequency gated by a temporal square envelope is optically injected to the FS fibre loop. The output signal unveils the resultant optically synthesized stepped-frequency signal. $E(t)$ denotes the electric field of the optical signals in the time domain. **c**, The optical coherent ranging principle is realized by mixing transmitted (solid lines

depicted in the time–frequency domain) and received (dashed lines) optical SF signals in a photodetector (PD). The demodulated RF signals after the PD are illustrated in the bottom panels, demonstrating the range at two distances, d_1 and d_2. $\Delta\tau_1$ and $\Delta\tau_2$ are the time delays introduced by the radar signal propagation with a speed of c. $I(t)$ denotes the demodulated signals (the photocurrent) after the photodetection in the time domain. **d**, Illustration of the use of the demonstrated photonic radar with millimetre resolution for detecting respiratory activities from multiple targets. OS, optical switch; FS, frequency-shifting. Δf, FS introduced by the AOFS.

Radar using radiofrequency (RF) waves can remotely access targets' vital signs to overcome the drawbacks of contact-based sensors. Vital sign information is produced based on RF sensing rather than camera filming, thus naturally providing the desired privacy protection. Electronic radar vital sign detection has recently been explored using single-tone and frequency-modulated waves. Single-tone radars that rely on the Doppler principle can acquire vital signs by obtaining the phase information of the reflected signal from a moving object. However, this technique lacks the facility to detect the roundtrip time and so access targets' range information. As a result, they cannot utilize range information to separate closely located targets and isolate a target from the surrounding clutter[16,17], which limits their performance and practicality in real-world deployment. In contrast, frequency-modulated radars can extract the range information to overcome this issue[18–21]. More importantly, the range resolution and accuracy of frequency-modulated radars can be increased by broadening the bandwidth of the sensing signals. Unfortunately, conventional electronic radar systems usually have limited sub-gigahertz bandwidths

that lead to a resolution of just tens of centimetres[22–24], which is insufficient to accurately detect delicate human vital sign signals (such as human respiration, with a chest displacement of ~1 cm). This limited resolution would greatly limit the capability to adequately cancel body motion and track multiple targets. Moreover, distributed sensing at multiple frequency bands and deployment locations is needed in emerging applications, but this is challenging for conventional electronics without a complicated parallel hardware architecture[25].

Microwave photonics-enabled radar technology is gaining momentum due to its numerous advantages over conventional electronic approaches for radar sensing[26,27]. Photonic radar systems have demonstrated their effectiveness in generating ultra-wideband signals, resulting in exceptional range resolution. Dispersion-based techniques offer bandwidths of up to 40 GHz, achieving fine resolutions down to 3.9 mm (ref. [28]). Frequency-sweeping light sources based on external optical injection have achieved a large time–bandwidth product exceeding 1.2×10^5, with longer pulse times improving signal-to-noise ratios in noisy environments, as well as overall performance[29]. Photonic
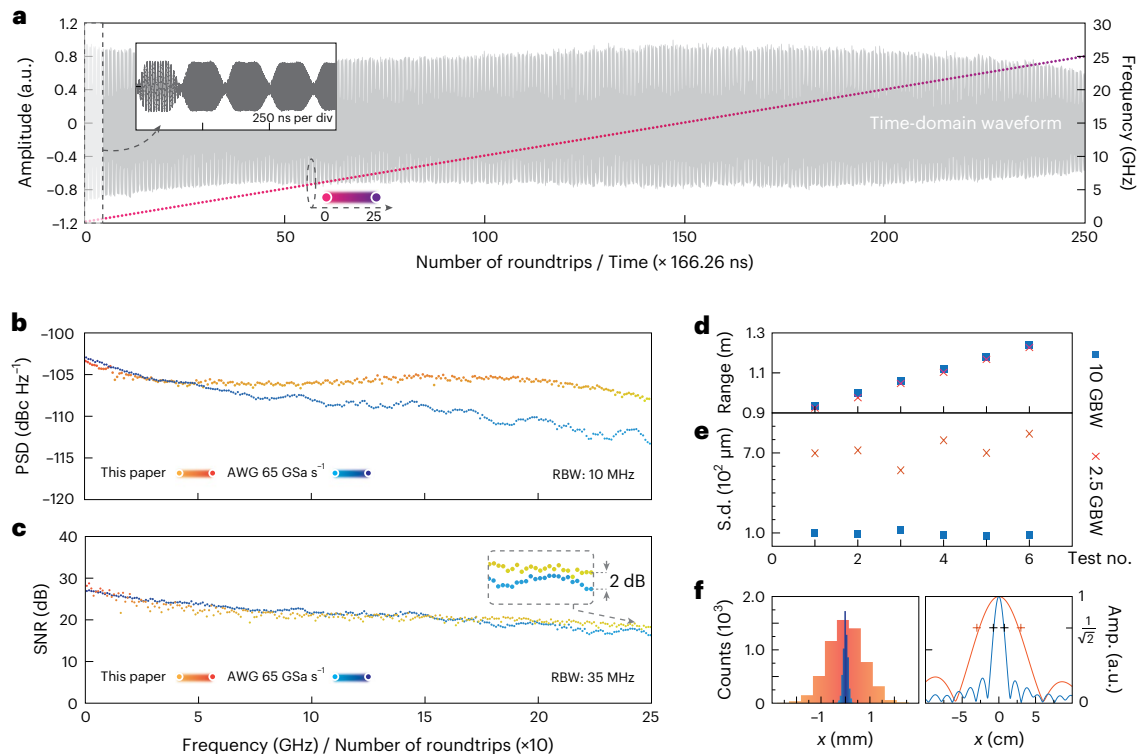
Fig. 2 | Radar signal and ranging quality analyses. a, The demonstrated SF waveform (left axis) and corresponding frequency (right axis), showing an overall bandwidth of 25 GHz. The completion time for the first injected pulse's nth roundtrip can be calculated by multiplying the number of roundtrips with the constant roundtrip time of 166.26 ns. **b**, Comparison of the demonstrated signal's PSD and an SF signal generated from an AWG with a sampling rate of 65 GSa s⁻¹. RBW, resolution bandwidth. **c**, SNR of signals generated by the demonstrated system and the AWG. **d,e**, Range (**d**) and accuracy in terms of s.d. (**e**) using 2.5-GHz- (crosses) and 10-GHz- (squares) bandwidth signals. **f**, S.d. values (left) of the 2.5-GHz (orange) and 10-GHz (blue) SF signals. Over 6,000 measurements, the 2.5-GHz and 10-GHz SF signals show s.d. values of 725.90 μm and 93.28 μm, respectively. Experimental (lines) and theoretical (−3 dB, plus symbols) range resolutions of the two signals are plotted accordingly.

frequency multiplication[30,31] and digital-to-analogue converters[32] provide a substantial bandwidth and high time–frequency linearity for accurate radar sensing. Photonic radar can generate different types of radar signal, including linear-frequency modulated (LFM)[33,34] and stepped-frequency (SF) signals[35–39]. Moreover, it can operate in multiple frequency bands across the millimetre-wave region, optimizing the performance based on operating conditions[40]. These features overcome the limitations of their electronic counterparts, making them well-suited to vital sign detection. However, despite its potential, photonic radar for vital sign detection has yet to be explored in real-world scenarios.

In this Article, we demonstrate a photonic radar for vital sign detection using human respiration simulators and a living animal—a cane toad—serving as a human proxy. The radar generates 10-GHz-wide SF RF signals in the Ka-band (26.5–40 GHz) to detect the respiratory activities of the simulators, achieving 13.7-mm range resolution with micrometre-level accuracy. This high resolution and accuracy are essential to resolve the delicate vital signs of the cane toad, even with an undersized animal radar cross-section. We demonstrated bandwidth scalability up to 30 GHz without the limitations of RF antennas and amplifiers. We also demonstrated a light detection and ranging (LiDAR) vital sign detection system based on the same microwave photonic source, showing the system's potential to enable the complementary features of radar and LiDAR. We envisage applying such a high-performance, distributed radar system in a range of healthcare scenarios, such as round-the-clock vital sign monitoring in aged-care facilities, hospitals and custodial settings. For example, a distributed photonic radar sensing network with multiple radar optical-RF access points can use RF waves to detect human vital signs

(Fig. 1a). This approach can continuously track uncooperative, back- or side-facing targets, unlike with the deployment of a single radar access point. As illustrated, one optical radar signal source enabling multiple optical-RF access points could cover diverse perspectives to monitor one or multiple targets using low-loss optical fibres.

An advanced SF photonic radar was constructed to detect the respiratory activities of humans and animals (Fig. 1b). The system mainly comprises an optical frequency-shifting fibre cavity to generate radar signals in the optical domain, an optical-fibre distribution network and optical-RF access points for electro-optic conversion and RF transceiving. In the frequency-shifting fibre cavity, an acousto-optic frequency shifter (AOFS) shifts the frequency of an optically injected pulse (with single frequency, f_c) by 100 MHz in each successive roundtrip ($\Delta f = 100$ MHz). An erbium-doped fibre amplifier (EDFA) inserted in the optical loop compensates for the power loss from optical propagation and coupling. This approach generates an optical SF signal consisting of a series of sine waves with linearly increased frequency in a precisely determined step (Fig. 1b,c). In the optical-RF access points, SF radar signals in the RF domain are generated through heterodyne mixing with a reference laser. The optical signal source only requires cost-effective and low-speed electronic devices (a dual-channel electrical function generator with an analogue bandwidth of 100 MHz) to precisely control the total synthesized bandwidth of the SF signal, which is tunable from the sub-gigahertz level to 30 GHz (Supplementary Section I). The function generator could be replaced by 100-MHz reference oscillators and RF switches with reduced complexity.

Radar vital sign detection starts by using the SF signal in the RF domain to illuminate a target area of interest (for example, the chest
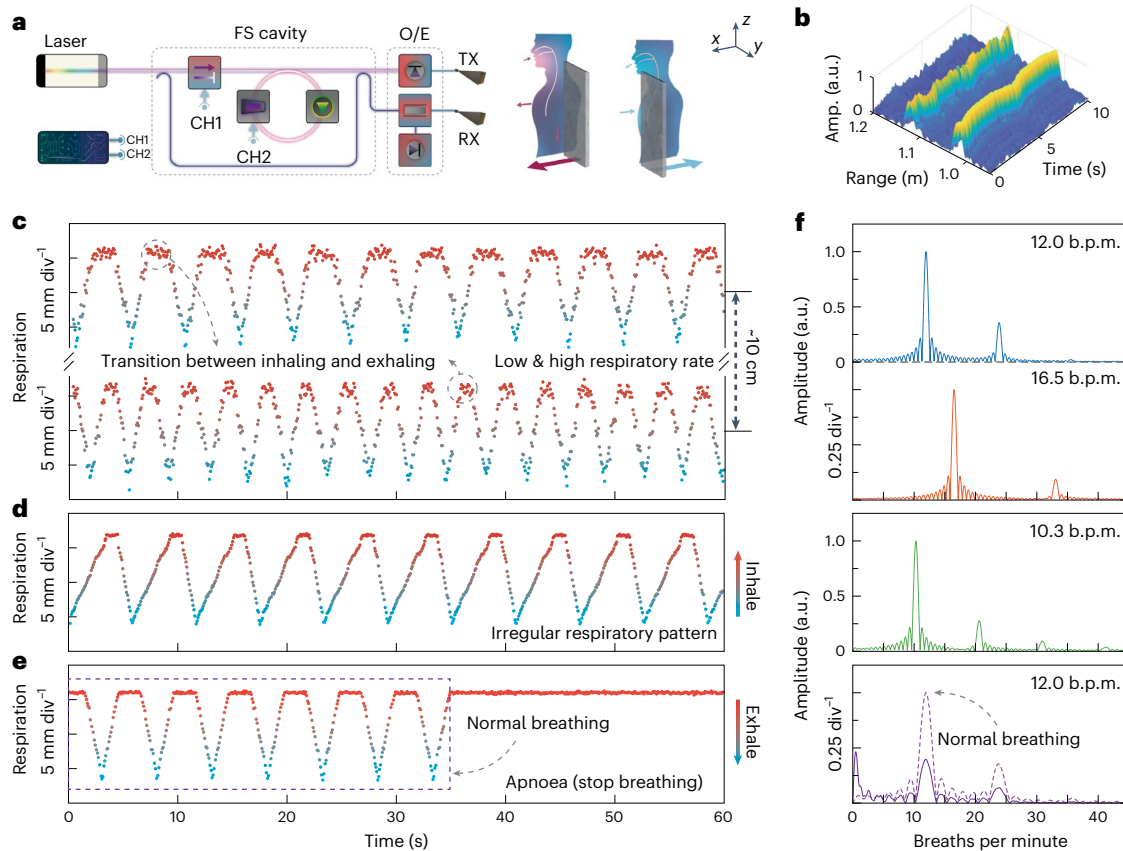
Fig. 3 | Multi-target vital sign detection results based on respiration simulators. a, Experimental set-up using the demonstrated photonic SF radar with an RF bandwidth of 10 GHz. Two metal plates ($4 \times 5 \times 0.3$ cm^3) separately mounted onto two stepper motors were used to emulate the chest movements of a human breathing. O/E denotes bidirectional conversions between the electrical and optical domains. **b**, Contactless vital sign detections of two closely located targets. **c**, Chest movements of the two targets. **d**, Chest movement showing irregular (longer inhalation and shorter exhalation) breathing patterns. **e**, Chest movement showing halted breathing, which could be a sign of apnoea. **f**, Fourier-transform results based on the chest movements in **c**–**e**.

area in humans) using a transmitting antenna element (TX). Another antenna element (RX) receives the reflected radar signals that carry the vital sign information, which are converted back to the optical domain using an electro-optic modulator (EOM). Demodulated SF signals are generated via a coherent detection process (Fig. 1c), that is, by optically mixing the transmitted reference signal (solid lines) with the received signal (dashed lines). Thus, targets at different ranges, for example, d_1 and d_2, have demodulated signals with different oscillating frequencies (Fig. 1c). These oscillating frequencies can be extracted through Fourier analysis, and show different peak locations in the frequency domain[37]. One advantage of using the SF signal format over other frequency-modulated approaches is that the radar receiver has a much lower sampling rate, which is favourable for fast signal processing, due to the fact that only one sample is required per roundtrip. For the same bandwidth, the SF signals sustain exactly the same resolution as other wideband radar waveforms (for example, LFM)[41]. As a result, such a system requires less computational power for digital signal processing (DSP), enabling real-time, multi-target respiration detection (Fig. 1d).
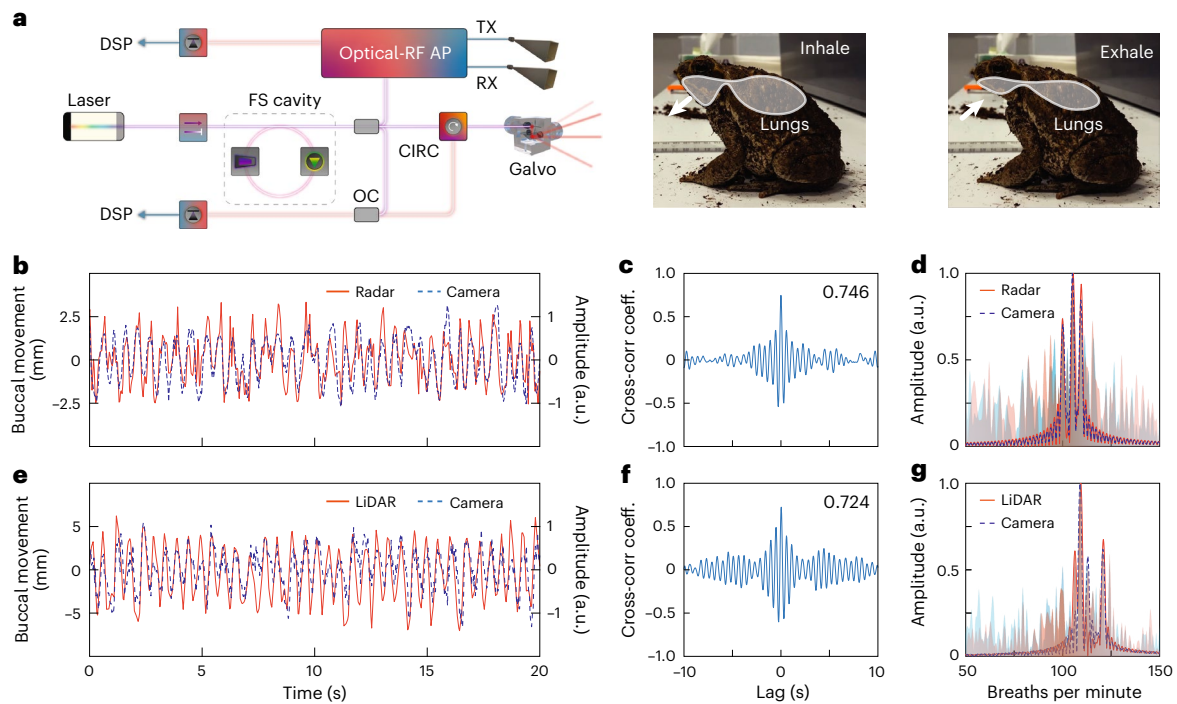
In a vital sign detection radar system, RF sensing signals with broader bandwidth and high time–frequency linearity[42] are required to maintain the range resolution and reduce measuring errors (increase accuracy). The signal (Fig. 2a) generated by the present frequency-shifting cavity demonstrated a bandwidth of 25 GHz, comparable to the signal generated by a digital arbitrary waveform generator (AWG) with 25-GHz analogue bandwidth. The frequency-shifting cavity has a roundtrip time of 162.26 ns with a constant 100-MHz frequency shift enabled by the AOFS. A total synthesized 25-GHz SF signal can be generated after the first injected pulse finishes 250 roundtrips in

the frequency-shifting cavity. High time–frequency linearity is inherited from the constant and stable AOFS-enabled frequency–time shifting[38], which is challenging to achieve using other photonics-based approaches[43,44].

The power spectral density (PSD) of the generated SF waveform maintains a constant level of around −103.7 dBc Hz^{-1} during the entire recirculation (Fig. 2b), only slightly reducing to −108.3 dBc Hz^{-1} on reaching the 250th circulation. In contrast, the PSD of the electronic counterpart exhibits noticeable degradation, from −103.0 dBc Hz^{-1} to −113.6 dBc Hz^{-1}, due to the AWG's limited analogue bandwidth. The signal-to-noise ratio (SNR) of the generated waveform was also calculated based on the PSD results (Methods), then compared with the signal generated by the AWG (Fig. 2c). The SNR results show no notable difference between these two signals across the 25-GHz bandwidth, proving that the demonstrated system could generate radar signals with AWG-comparable quality. It is worth mentioning that the signal quality is not expected to deteriorate with photonics-based upconversion, unlike with conventional electronic upconversion[45,46].

We also investigated the range resolution (Fig. 2d) and accuracy (characterized as the standard deviation, s.d.; Fig. 2e) of the vital sign-detection photonic radar system. The results were taken for SF signals with 2.5-GHz (crosses) and 10-GHz (squares) bandwidths based on a metal plane reflector with dimensions of $4 \times 5 \times 0.3$ cm^3 (Methods). The SF signal with wider bandwidth (10 GHz) shows a significant accuracy improvement compared with the narrower-bandwidth (2.5 GHz) signal (Fig. 2f), showing a reduction in s.d. to 93.28 μm from 725.90 μm based on signals with experimental range resolutions of 13.7

Fig. 4 | Vital sign detection results using a cane toad as a human proxy.
a, Experimental set-up using the demonstrated system for radar sensing, which also shows its flexibility and capability for LiDAR detection. **b**, Experimental results for detecting the buccal-cavity movement of a cane toad using the demonstrated radar system. Camera-extracted data were used as a reference. **c**, Cross-correlation between the radar and camera data, showing a coefficient of 0.746. **d**, Frequency-domain analyses of the radar (red shadow) and camera (blue shadow) data with three top-weighted Fourier coefficients in solid and dashed lines, respectively. **e**, Experimental results for detecting the buccal-cavity movement of the cane toad using a LiDAR system. **f**, Cross-correlation between the LiDAR and camera data, showing a coefficient of 0.724. **g**, Frequency-domain analyses of the LiDAR (red shadow) and camera (blue shadow) data with three top-weighted Fourier coefficients in solid and dashed lines, respectively. OC, optical coupler; CIRC, optical circulator; Galvo, 2D scanning mirrors. The cross-correlation and frequency-domain analyses use time-domain data longer than the data shown in **b** and **e**.

and 53.2 mm, respectively. These results prove that increasing the sensing signal bandwidth will simultaneously improve the range resolution and accuracy, which is greatly desirable in a radar system used to detect delicate respiratory activities from multiple targets.

Next, we applied the photonic radar to multi-target respiration detection using two simulators of human breathing (Fig. 3a). Our radar successfully detected the respiratory activities of two closely located targets (~10 cm apart) in real time (Fig. 3b). Over a 60-s time window, the relative chest movements of the two targets were extracted (Fig. 3c). The corresponding respiratory frequencies, in units of b.p.m., were acquired by taking the Fourier transform of the trajectories (Fig. 3f), finding respiratory rates (RRs) of 12 b.p.m. and 16.5 b.p.m. for the two targets, respectively. These two frequencies were chosen deliberately to match the typical RR of an adult at rest[47–49]. The superior accuracy of our system also allows the radar system to detect irregular respiration patterns from subtle movements (around the millimetre level), such as irregular breathing with longer inhalations and shorter exhalations, as well as halts in breathing (Fig. 3d,e). It can thus help accurately identify or even predict respiratory abnormalities linked to many medical conditions, such as asthma, anxiety, congestive heart failure and lung disease[48]. The demonstrated results indeed prove that the accuracy of the demonstrated system offers sufficient precision to pick up respiratory abnormalities.

To prove its suitability for practical applications, we demonstrated animal respiratory detection using a female cane toad as a human proxy (a pilot study before human trials) to evaluate the performance of the radar (Fig. 4a). The cane toad has a radar cross-section (the buccal area, ~2 × 2.5 cm²) that is smaller than the human chest, making the experiment more challenging than human trials. The buccal cavity is connected to the lungs during its breathing activity[50–52]. The toad was located ~1 m from the radar antenna, with the beam pointing to the toad's buccal area. The data extracted from the photonic radar produced a real-time trace of the toad's buccal movement, which had a displacement of ~5 mm (Fig. 4b). The radar data were then cross-referenced with data extracted from a simultaneously recorded video clip, giving a cross-correlation coefficient of 0.746 (Fig. 4c). It is worth mentioning that the camera had a different perspective from the radar beam direction, which might have slightly decreased the correlation coefficient (Supplementary Section IX). Fourier-domain analyses based on the radar and camera data further proved the accuracy and performance of the photonics-enabled radar system (Fig. 4d). The respiration data show that the cane toad has an irregular respiration pattern—intermittent or discontinuous breathing patterns (Supplementary Section X) are common in amphibians[50–52]—which agrees with both the radar and camera-based results.

The proposed radar system can also be adopted for LiDAR sensing (Fig. 4a), where RF components such as RF amplifiers and antennas no longer limit the system's bandwidth. The demonstrated scheme enabled a LiDAR system with a total synthesized bandwidth of 25 GHz (6-mm range resolution), sufficient to catch the toad's buccal movements (Fig. 4e). This was validated by cross-referencing the LiDAR data with camera data using cross-correlation (Fig. 4f) and Fourier analyses (Fig. 4g). We have thus provided an approach to achieve a hybrid radar–LiDAR system that combines complementary detection techniques for improved sensing accuracy and system resilience.

In summary, we have demonstrated a photonic vital sign detection system with fine resolution down to 6 mm and micrometre-level accuracy, enabling multi-target detection without comfort and privacy issues. Experimental validations have proved its ability and effectiveness in picking up delicate respiratory abnormalities and accurately extracting a cane toad's buccal movements. More importantly, it has a simplified

system structure that provides improved bandwidth and flexibility that are not achievable by current state-of-the-art electronic vital sign radars without requiring parallel or multiplexed electronic architectures.

The system can support radar and LiDAR sensing, proving its unprecedented flexibility and potential for hybrid detection and sensor abilities, which offer more consistent and accurate sensing results[53]. The radar system operates similarly to LiDAR, as both rely on the same ranging and detection principle. Radar uses radio waves instead of light waves, resulting in better penetration through clothes and thin walls. However, the longer wavelength (typically centimetre-level) of radio waves makes it harder to confine the signal, leading to a lack of spatial information, and requiring a larger antenna to improve gain and directionality. The larger beam size of radar systems, compared to LiDAR, increases their vulnerability to reflections from surrounding clutter, crosstalk with other vital sign radar systems, and interference from unknown RF signals in the same frequency band. On the other hand, LiDAR, which uses light, with its much shorter wavelengths, has a superior range and spatial resolution due to its broader sensing bandwidth and 2D scanning capabilities. However, it is more difficult for LiDAR to see through (penetration ability) objects such as clothes due to its micrometre optical wavelength. Accordingly, LiDAR is a complementary approach that can be used to assist radar in detecting vital signs.

The proposed radar system can maximize its bandwidth potential via the integration of available photonic and RF technologies, including the use of commercially available components such as the uni-travelling-carrier photodiode with its frequency range of up to 900 GHz and a bandwidth exceeding 340 GHz (refs. 54,55), as well as RF amplifiers[56] and antennas designed for compatible frequencies. Furthermore, it is compatible with the photonic distributed, multi-band-operation radar technique[25]. Thus, multiple sensors, enabled by one centralized photonic system, can seamlessly work together without interference to achieve broader detection coverage with lower overall complexity and cost. In terms of future developments towards the miniaturization of photonic systems, recent advances in the photonic integration of critical function building blocks, such as on-chip AOFSs[57,58] and optical waveguide amplifiers[59,60], are providing a promising technical basis with which to achieve compact size for portable sensing[31,53]. This photonic approach offers a new path towards high-resolution, rapid-response and cost-effective hybrid radar–LiDAR modules for distributed, contactless vital sign detection.

Online content

Any methods, additional references, Nature Portfolio reporting summaries, source data, extended data, supplementary information, acknowledgements, peer review information; details of author contributions and competing interests; and statements of data and code availability are available at https://doi.org/10.1038/s41566-023-01245-6.

References

1. Cardillo, E. & Caddemi, A. A review on biomedical MIMO radars for vital sign detection and human localization. *Electronics* **9**, 1497 (2020).
2. Dunn, J. et al. Wearable sensors enable personalized predictions of clinical laboratory measurements. *Nat. Med.* **27**, 1105–1112 (2021).
3. Ren, L. et al. Comparison study of noncontact vital signs detection using a Doppler stepped-frequency continuous-wave radar and camera-based imaging photoplethysmography. *IEEE Trans. Microw. Theory Tech.* **65**, 3519–3529 (2017).
4. Mercuri, M. et al. Frequency-tracking CW Doppler radar solving small-angle approximation and null point issues in non-contact vital signs monitoring. *IEEE Trans. Biomed. Circuits Syst.* **11**, 671–680 (2017).
5. Massaroni, C. et al. Respiratory monitoring during physical activities with a multi-sensor smart garment and related algorithms. *IEEE Sensors J.* **20**, 2173–2180 (2020).
6. Daniela, L. P. et al. A multi-parametric wearable system to monitor neck movements and respiratory frequency of computer workers. *Sensors* **20**, 536 (2020).
7. Liu, H., Allen, J., Zheng, D. & Chen, F. Recent development of respiratory rate measurement technologies. *Physiol. Meas.* **40**, 07TR01 (2019).
8. Bennett, S., Nasser El Harake, T., Goubran, R. & Knoefel, F. Adaptive Eulerian video processing of thermal video: an experimental analysis. *IEEE Trans. Instrum. Meas.* **66**, 2516–2524 (2017).
9. Chaichulee, S. et al. Multi-task convolutional neural network for patient detection and skin segmentation in continuous non-contact vital sign monitoring. In *Proc. 12th IEEE International Conference on Automatic Face & Gesture Recognition (FG 2017)* 266–272 (IEEE, 2017).
10. Lyra, S. et al. A deep learning-based camera approach for vital sign monitoring using thermography images for ICU patients. *Sensors* **21**, 1495 (2021).
11. Aarts, L. A. M. et al. Non-contact heart rate monitoring utilizing camera photoplethysmography in the neonatal intensive care unit—a pilot study. *Early Human Dev.* **89**, 943–948 (2013).
12. Kumar, M., Veeraraghavan, A. & Sabharwal, A. DistancePPG: robust non-contact vital signs monitoring using a camera. *Biomed. Opt. Express* **6**, 1565–1588 (2015).
13. Fleck, S. & Strasser, W. Smart camera based monitoring system and its application to assisted living. *Proc. IEEE* **96**, 1698–1714 (2008).
14. Akter, T., Dosono, B., Ahmed, T., Kapadia, A. & Semaan, B. 'I am uncomfortable sharing what I can't see': privacy concerns of the visually impaired with camera based assistive applications. In *Proc. 29th USENIX Security Symposium (USENIX Security 20)* 1929–1948 (USENIX Association, 2020).
15. Al-Turjman, F., Zahmatkesh, H. & Shahroze, R. An overview of security and privacy in smart cities' IoT communications. *Trans. Emerging Telecommun. Technol.* **33**, 3677 (2022).
16. Li, C., Lubecke, V. M., Boric-Lubecke, O. & Lin, J. A review on recent advances in Doppler radar sensors for noncontact healthcare monitoring. *IEEE Trans. Microw. Theory Tech.* **61**, 2046–2060 (2013).
17. Tu, J., Hwang, T. & Lin, J. Respiration rate measurement under 1-D body motion using single continuous-wave Doppler radar vital sign detection system. *IEEE Trans. Microw. Theory Tech.* **64**, 1937–1946 (2016).
18. Wang, G., Munoz-Ferreras, J. M., Gu, C., Li, C. & Gomez-Garcia, R. Application of linear-frequency-modulated continuous-wave (LFMCW) radars for tracking of vital signs. *IEEE Trans. Microw. Theory Tech.* **62**, 1387–1399 (2014).
19. Quaiyum, F., Ren, L., Nahar, S., Foroughian, F. & Fathy, A. E. Development of a reconfigurable low cost multi-mode radar system for contactless vital signs detection. In *Proc. 2017 IEEE MTT-S International Microwave Symposium (IMS)* 1245–1247 (IEEE, 2017).
20. Ahmad, A., Roh, J. C., Wang, D. & Dubey, A. Vital signs monitoring of multiple people using a FMCW millimeter-wave sensor. In *Proc. 2018 IEEE Radar Conference (RadarConf18)* 1450–1455 (IEEE, 2018).
21. Mercuri, M. et al. Vital-sign monitoring and spatial tracking of multiple people using a contactless radar-based sensor. *Nat. Electron.* **2**, 252–262 (2019).
22. Wang, Y., Liu, Q. & Fathy, A. E. CW and pulse-Doppler radar processing based on FPGA for human sensing applications. *IEEE Trans. Geosci. Remote Sensing* **51**, 3097–3107 (2013).
23. Su, W. C., Tang, M. C., Arif, R. E., Horng, T. S. & Wang, F. K. Stepped-frequency continuous-wave radar with self-injection-locking technology for monitoring multiple human vital signs. *IEEE Trans. Microw. Theory Tech.* **67**, 5396–5405 (2019).

24. Fang, G. W., Huang, C. Y. & Yang, C. L. Switch-based low intermediate frequency system of a vital sign radar for simultaneous multitarget and multidirectional detection. *IEEE J. Electromagn. RF Microw. Med. Biol.* **4**, 265–272 (2020).

25. Serafino, G. et al. A photonics-assisted multi-band MIMO radar network for the port of the future. *IEEE J. Sel. Topics Quantum Electron.* **27**, 1–13 (2021).

26. Pan, S. et al. Microwave photonic radars. *J. Light. Technol.* **38**, 5450–5484 (2020).

27. Hao, T. et al. Recent advances in optoelectronic oscillators. *Adv. Photonics* **2**, 044001 (2020).

28. Li, Y. et al. Photonic generation of W-band arbitrary waveforms with high time-bandwidth products enabling 39-mm range resolution. *Optica* **1**, 446–454 (2014).

29. Zhou, P., Zhang, F., Guo, Q. & Pan, S. Linearly chirped microwave waveform generation with large time-bandwidth product by optically injected semiconductor laser. *Opt. Express* **24**, 18460–18467 (2016).

30. Zhang, F. et al. Photonics-based broadband radar for high-resolution and real-time inverse synthetic aperture imaging. *Opt. Express* **25**, 16274–16281 (2017).

31. Li, S. et al. Chip-based microwave-photonic radar for high-resolution imaging. *Laser Photon. Rev.* **14**, 1900239 (2020).

32. Peng, S. et al. High-resolution W-band ISAR imaging system utilizing a logic-operation-based photonic digital-to-analog converter. *Opt. Express* **26**, 1978–1987 (2018).

33. Cheng, R., Wei, W., Xie, W. & Dong, Y. Photonic generation of programmable coherent linear frequency modulated signal and its application in X-band radar system. *Opt. Express* **27**, 37469–37480 (2019).

34. Tang, J. et al. Hybrid Fourier-domain mode-locked laser for ultra-wideband linearly chirped microwave waveform generation. *Nat. Commun.* **11**, 3814 (2020).

35. Zhang, Z., Liu, Y., Burla, M. & Eggleton, B. J. 5.6-GHz-bandwidth photonic stepped-frequency radar using MHz-level frequency-shifting modulation. In *Proc. 2020 Conference on Lasers and Electro-Optics (CLEO)* 1–2 (IEEE, 2020).

36. Zhang, Y. et al. Multi-functional radar waveform generation based on optical frequency-time stitching method. *J. Light. Technol.* **39**, 458–464 (2021).

37. Liu, Y., Zhang, Z., Burla, M. & Eggleton, B. J. 11-GHz-bandwidth photonic radar using MHz electronics. *Laser Photon. Rev.* **16**, 2100549 (2022).

38. Zhang, Z., Liu, Y. & Eggleton, B. Photonic generation of 30 GHz bandwidth stepped-frequency signals for radar applications. *J. Light. Technol.* **40**, 4521–4527 (2022).

39. Lyu, Y. et al. Photonic generation of highly-linear ultra-wideband stepped-frequency microwave signals with up to $6 \cdot 10^6$ time-bandwidth product. *J. Light. Technol.* **40**, 1036–1042 (2022).

40. Ghelfi, P., Laghezza, F., Scotti, F., Onori, D. & Bogoni, A. Photonics for radars operating on multiple coherent bands. *J. Light. Technol.* **34**, 500–507 (2016).

41. Ozdemir, C. *Inverse Synthetic Aperture Radar Imaging with MATLAB Algorithms* (Wiley, 2021).

42. Ayhan, S. et al. Impact of frequency ramp nonlinearity, phase noise, and SNR on FMCW radar accuracy. *IEEE Trans. Microw. Theory Tech.* **64**, 3290–3301 (2016).

43. Hao, T. et al. Breaking the limitation of mode building time in an optoelectronic oscillator. *Nat. Commun.* **9**, 1839 (2018).

44. Zhou, P., Zhang, R., Li, N., Jiang, Z. & Pan, S. An RF-source-free reconfigurable microwave photonic radar with high-resolution and fast detection capability. *J. Light. Technol.* **40**, 2862–2869 (2022).

45. Ho, S. S. K. & Saavedra, C. E. A CMOS broadband low-noise mixer with noise cancellation. *IEEE Trans. Microw. Theory Tech.* **58**, 1126–1132 (2010).

46. Jankiraman, M. *FMCW Radar Design* (Artech House, 2018).

47. Chioukh, L., Boutayeb, H., Wu, K. & Deslandes, D. Monitoring vital signs using remote harmonic radar concept. In *Proc. 2011 41st European Microwave Conference* 1269–1272 (IEEE, 2011).

48. Schriger, D.L. in *Goldman's Cecil Medicine* Vol. 1 (eds Goldman, L & Schafer, A.I.) Ch. 7, 27–30 (Elsevier, 2020).

49. Nahar, S. et al. An electromagnetic model of human vital signs detection and its experimental validation. *IEEE J. Emerging Selected Topics Circuits Syst.* **8**, 338–349 (2018).

50. Stinner, J. N. & Hartzler, L. K. Effect of temperature on pH and electrolyte concentration in air-breathing ectotherms. *J. Exp. Biol.* **203**, 2065–2074 (2000).

51. Reid, S. G., Milsom, W. K., Meier, J. T., Munns, S. & West, N. H. Pulmonary vagal modulation of ventilation in toads (*Bufo marinus*). *Resp. Physiol.* **120**, 213–230 (2000).

52. Jenkin, S. E. M. *The effect of temperature on the chronic hypoxia-induced changes to pH/CO_2-sensitive fictive breathing in the cane toad (Bufo marinus)*. MSc thesis, Ottawa: Library and Archives Canada (2012).

53. Falconi, F. et al. A combined radar & LiDAR system based on integrated photonics in silicon-on-insulator. *J. Light. Technol.* **39**, 17–23 (2021).

54. Nagatsuma, T., Ito, H. & Ishibashi, T. High-power RF photodiodes and their applications. *Laser Photon. Rev.* **3**, 123–137 (2009).

55. Kurokawa, T., Ishibashi, T., Shimizu, M., Kato, K. & Nagatsuma, T. Over 300 GHz bandwidth UTC-PD module with 600 GHz band rectangular-waveguide output. *Electron. Lett.* **54**, 705–706 (2018).

56. Camarchia, V. et al. A review of technologies and design techniques of millimeter-wave power amplifiers. *IEEE Trans. Microw. Theory Tech.* **68**, 2957–2983 (2020).

57. Shao, L. et al. Integrated lithium niobate acousto-optic frequency shifter. In *Proc. Conference on Lasers and Electro-Optics* STh1F.5 (Optica Publishing Group, 2020).

58. Yu, Z. & Sun, X. Gigahertz acousto-optic modulation and frequency shifting on etchless lithium niobate integrated platform. *ACS Photonics* **8**, 798–803 (2021).

59. Vagionas, C. et al. Lossless 1×4 silicon photonic ROADM based on a monolithic integrated erbium doped waveguide amplifier on a Si_3N_4 platform. *J. Light. Technol.* **40**, 1718–1725 (2022).

60. Liu, Y. et al. A photonic integrated circuit-based erbium-doped amplifier. *Science* **376**, 1309–1313 (2022).

Methods

Baseband RF signals were acquired by mixing the optical SF signal with a tap of the c.w. laser in a 50-GHz PD. A real-time oscilloscope, with a sampling speed of 80 GSa s^{-1}, measured the time-domain data in Fig. 2. Each time and frequency data point was extracted based on a 100-ns time window located in the middle of each frequency step.

The PSD shown in Fig. 2b was estimated by employing a one-sided periodogram. Each PSD estimation utilized a 100-ns time-domain segment containing 8,000 data points, employing a rectangular window and a resolution bandwidth of 10 MHz. The SNR presented in Fig. 2c was estimated using a one-sided power spectrum, employing a 100-ns time-domain segment with 8,000 data points and a Kaiser window (shape factor $\beta = 38$). This approach maximized the energy concentration in the main lobe and resulted in an equivalent rectangular noise bandwidth of 35.08 MHz.

The ranging results were measured using 2.5-GHz and 10-GHz stepped-frequency waveforms to illuminate a metal plane reflector with dimensions of $4 \times 5 \times 0.3$ cm^3. The reflected RF signal was converted to the optical domain via a phase modulator and mixed with a tap of the transmitted optical SF signal for coherent optical detection in a PD, forming an RF demodulated signal (Fig. 1c). Another low-speed real-time oscilloscope sampled the demodulated signal with a sampling rate (1.25 GSa s^{-1}) greater than the inverse of the roundtrip time to ensure a minimum of one sample per frequency step. The demodulated signal was used in DSP. For example, the 10-GHz SF signal had 100 steps, so 100 data points were used for extracting the range information. Each ranging result had a Fourier-transform-limited resolution of 46 μm using a 2^{15}-point (inverse) Fourier transform. Each data point in Fig. 2d was obtained by extracting 1,000 individual range measurements for the same stationary target. This 1,000-time range measurement process was repeated at varying distances, with a 6-cm spacing between each distance and an estimated human placement error of ~1 mm.

Data availability

The data that support the plots within this paper are available at https://doi.org/10.5281/zenodo.7896142 (ref. 61). Any other data and findings of this study are available from the corresponding author upon reasonable request.

Code availability

The data-processing code used to produce the plots within this paper is available at https://doi.org/10.5281/zenodo.7896142 (ref. 61).

Reference

61. Zhang, Z., Liu, Y., Stephens, T. & Eggleton, B. J. Photonic radar for contactless vital sign detection. *Zenodo* https://doi.org/10.5281/zenodo.7896142 (2023).

Author contributions

Y.L. and B.J.E. conceived the project. Y.L. and Z.Z. designed the system structure. Z.Z. conducted the experiments. Z.Z. and T.S. conducted the animal experiments. Z.Z., Y.L. and T.S. performed the data analysis. Z.Z. and Y.L. wrote the manuscript with contributions from B.J.E. and T.S. Y.L. and B.J.E. supervised the project.

Competing interests

The authors declare no competing interests.

Animal ethics

All animal experiments were performed under the Animal Research Authority, project number 2022/2090, approved by the Animal Ethics Committee (AEC), the University of Sydney, in compliance with Section 27 of the NSW *Animal Research Act 1985*.

Additional information

Supplementary information The online version contains supplementary material available at https://doi.org/10.1038/s41566-023-01245-6.

Correspondence and requests for materials should be addressed to Yang Liu or Benjamin J. Eggleton.

Peer review information *Nature Photonics* thanks Alexander Cerjan and the other, anonymous, reviewers for their contribution to the peer review of this work.

Reprints and permissions information is available at www.nature.com/reprints.